On the lumped capacitance approximation accuracy in RC network building models[☆]

Kevin J. Kircher[a], K. Max Zhang[a,*]

[a]*Sibley School of Mechanical and Aerospace Engineering, Cornell University, Ithaca, NY, USA*

Abstract

Thermal resistor-capacitor networks are a popular method for control-oriented building modeling. A basic assumption underlying this method is that the continuous temperature distribution in a wall or window is well-approximated by a small number of lumped capacitances. In this paper, we explore the accuracy of this approximation when a single capacitance is used. We derive conditions on the dimensionless parameters that characterize the problem, called Biot numbers, that lead to small errors in approximating a wall or window's surface heat fluxes and internal energy. The lumped capacitance approximation can be surprisingly accurate for Biot numbers much larger than the conventional upper bound of 0.1. In particular, the approximation is nearly exact for window panes, and is often acceptable for uniform walls. A large Biot number at an indoor wall surface, however, leads to large lumped capacitance approximation errors.

Keywords: lumped capacitance approximation, RC networks, MPC, HVAC

1. Introduction

Buildings consumed 41% of U.S. primary energy in 2010, at a cost of $448 billion and 7% of the world's greenhouse gas emissions. [1] Over half of the energy consumed in U.S. buildings goes toward heating, ventilation and air conditioning (HVAC). [2, 3] The opportunities for improving HVAC controls are significant: a 2005 study estimated that sophisticated controls could reduce the U.S. commercial sector's energy expenditures by 13% at relatively low capital costs. [4]

Model predictive control (MPC), an optimization-based method widely used in the chemical processing and automotive industries [5], has shown promise in HVAC applications. In 2011, a two-week deployment of MPC for radiant heating on a university campus reported upwards of 15% savings in HVAC energy relative to standard controls. [6] In 2012, MPC was deployed in a six-story office building, actuating temperature and flow rate setpoints and the angles of controllable blinds. [7] The system ran smoothly for the full three-month trial with no complaints from building occupants; supporting simulations estimated 17% HVAC energy savings. Another 2012 MPC study in an office building estimated 60% energy savings over a five day trial. [8] Many simulation studies have predicted improvements on par with these early experimental results. [9]

A significant barrier to widespread adoption of MPC for HVAC systems is the need for a building model. [10] To be useful for MPC, such a model must (1) accurately predict indoor air temperatures as a function of weather, internal heat gains, and control actions, and (2) easily interface with an optimization solver. Existing building simulators such as EnergyPlus and TRNSYS meet the first criterion, but fail the second; although they can technically interface with scientific computing environments capable of optimization, the integration process requires complicated middleware, and the optimization can be slow and unreliable. These facts motivate the current research effort to develop control-oriented building modeling software. Three promising approaches are neural networks, autoregressive processes, and resistor-capacitor (RC) networks. [11] This paper focuses on RC networks, which are gray-box models that have shown surprisingly good predictive power

[☆]This is a pre-print. The final version will appear in *Energy and Buildings* in late 2015.

*Corresponding author: kz33@cornell.edu, (607) 254-5402.

in many studies. [12, 13, 14, 15, 16, 7] We wish to understand this success, and to inform RC network modeling by highlighting cases where the RC network loses its physical meaning.

RC networks aim to capture the dominant building physics, while ignoring the nonlinearities that complicate controller design. The typical approach, as described in §2 of [17], is to assign a thermal capacitance to each wall (or window, floor, or ceiling) and to the air in each room. Each air node is connected to the adjacent wall nodes through a thermal resistance. Heat transfer between air and wall nodes is assumed to be linear, and coupling between walls is ignored. The resulting model is a linear, time-invariant dynamical system whose states are the node temperatures. The model parameters may be assigned using *a priori* knowledge of the building, or estimated from data.

The RC network approach involves three major assumptions:

1. radiative coupling between surfaces is negligible,
2. air-wall convection is linear, and
3. the continuous temperature distribution inside a wall can be approximated by a small number of lumps of uniform temperature.

Assumption 1 is reasonable for interior wall surfaces, which are often nearly isothermal with one another. It is less accurate for coupling between interior and exterior walls. Assumption 2 is a common model of convection, but can also introduce error; for example, film coefficients for natural convection along vertical walls vary with the cube root of the driving temperature gradient. [18] RC network models ignore such mild nonlinearities. Assumption 3 is the focus of this paper.

The overall goal of our study is to understand the applicability of RC network models in order to enhance the capabilities of MPC in buildings. Specifically, we aim to quantify the lumped capacitance approximation accuracy in the RC network setting. For tractability, we restrict our attention to the case where a uniform wall or window is modeled as a single lumped capacitance, and where Assumptions 1 and 2 are accurate. We begin in §2 by formally stating the problem and reviewing related work (§2.1), deriving the lumped capacitance approximation (§2.2), defining error metrics (§2.3), and presenting the analytical solution (§2.4). The accuracy results in §3 include both steady state (§3.1) and transient (§3.2) regimes; we apply the results to two examples in §3.3 and conclude in §4. Mathematical details and a summary of notation can be found in the appendices.

2. Theory

2.1. Problem statement and related work

The lumped capacitance approximation eliminates spatial variation from transient conduction, reducing the heat equation

$$\frac{\partial T}{\partial t} = \alpha \frac{\partial^2 T}{\partial x^2}$$

to an ordinary differential equation in time. Introductory heat transfer textbooks commonly present the lumped capacitance approximation as the first method for analyzing transient conduction, along with the rule of thumb that the approximation is accurate for Biot numbers less than 0.1. [19, 20, 21] The method is often justified through the example of a small, highly conductive object symmetrically cooled by convection to a surrounding fluid. We wonder whether the "Bi $\leq$ 0.1" rule of thumb extends to the asymmetric situations that arise in buildings.

To explore this question, we consider the uniform, one-dimensional slab shown in Figure 1. We assume that all thermal properties, including the heat transfer coefficients at either surface, are spatially uniform and independent of temperature. The two sides of the slab are exposed to the driving temperatures T_0 and T_l, with heat exchange governed by the coefficients h_0 and h_l (W/m^2·K). The surfaces gain or lose the fluxes $\tilde{q}_0$ and $\tilde{q}_l$ (W/m^2) through temperature-independent mechanisms, such as shortwave radiation or heat sources or sinks. This gives the net surface fluxes

$$\begin{aligned} q_0(t) &= h_0(T_0 - T(0,t)) + \tilde{q}_0 \\ q_l(t) &= h_l(T(l,t) - T_l) + \tilde{q}_l, \end{aligned} \tag{1}$$

with fluxes to the right defined to be positive. We seek to quantify the accuracy of the lumped capacitance approximation to the true solution of the problem

$$\begin{aligned} &\frac{\partial T}{\partial t} = \alpha \frac{\partial^2 T}{\partial x^2}, \quad x \in [0,l],\ t \geq 0 \\ &T(x,0) = T_i, \quad x \in [0,l] \\ &\left.\frac{\partial T}{\partial x}\right|_{0,t} = -\frac{q_0(t)}{k}, \quad \left.\frac{\partial T}{\partial x}\right|_{l,t} = -\frac{q_l(t)}{k}, \quad t \geq 0, \end{aligned} \tag{2}$$

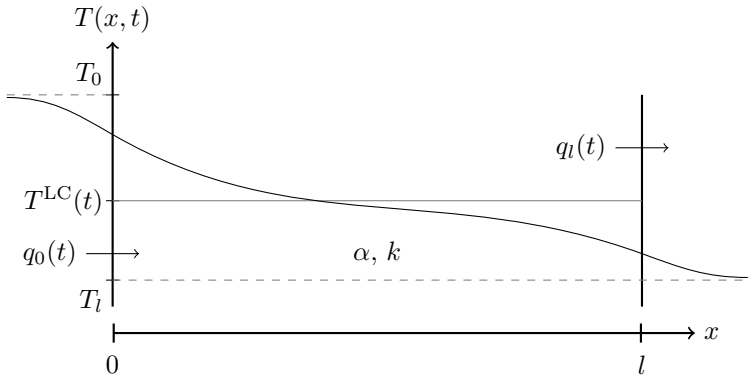

Figure 1: a uniform slab of length l, thermal diffusivity α, and thermal conductivity k. The net heat fluxes $q_0(t)$ and $q_l(t)$ depend on the surface temperatures $T(0,t)$ and $T(l,t)$ and the driving temperatures T_0 and T_l. The lumped capacitance approximation of $T(x,t)$ is $T^{\mathrm{LC}}(t)$.

where T_i is the initial temperature of the slab.

In 2001, Alhama and Campo studied a special case of this problem with $T_0 = T_l$ and $\tilde{q}_0 = \tilde{q}_l = 0$, so that all asymmetry was in the heat transfer coefficients $h_0 \neq h_l$. [22] By comparing the lumped capacitance model to the output of the circuit simulation code PSPICE, they sketched out a region of the Biot numbers $\mathrm{Bi}_0 \equiv h_0 l/k$ and $\mathrm{Bi}_l \equiv h_l l/k$ that maintain the error metric $\gamma_{\mathrm{AC}}(t)$, defined in §2.3, under 5% for all $t \geq 0$. The boundaries of this set are the dashed black lines in Figures 5 through 9.

This paper extends Alhama and Campo's work by considering a more general problem, by benchmarking against the analytical solution rather than a circuit simulator, and by exploring the evolution of the approximation accuracy with time. New error metrics are defined that, compared to γ_{AC}, more closely reflect the physical quantities of interest in applications (*e.g.*, surface fluxes and stored energy), as well as the underlying assumptions of the lumped capacitance approximation. We provide plots from which the reader can easily quantify the approximation accuracy by each error metric and for a wide range of time scales. We give numerical conditions on the Biot numbers that keep all error metrics under 5, 10, ..., and 35% for all time.

2.2. The lumped capacitance approximation

The heat equation for the uniform slab in Figure 1 can be written as

$$\frac{\partial T}{\partial t} = \alpha \frac{\partial}{\partial x}\left(\frac{\partial T}{\partial x}\right), \quad x \in [0,l],\ t \geq 0.$$

Integrating both sides over x from 0 to l gives

$$\frac{\mathrm{d}}{\mathrm{d}t}\int_0^l T(x,t)\mathrm{d}x = \alpha\left(\left.\frac{\partial T}{\partial x}\right|_{l,t} - \left.\frac{\partial T}{\partial x}\right|_{0,t}\right), \tag{3}$$

where the left-hand side follows from Leibniz's integral rule and the right-hand side from the fundamental theorem of calculus. The left-hand side of equation (3) is the scaled time derivative of the spatial average temperature $\bar{T}(t) \equiv (1/l)\int_0^l T(x,t)\mathrm{d}x$. By Fourier's law, the terms on the right-hand side of (3) are

$$\left.\frac{\partial T}{\partial x}\right|_{0,t} = -\frac{q_0(t)}{k}, \quad \left.\frac{\partial T}{\partial x}\right|_{l,t} = -\frac{q_l(t)}{k},$$

so (3) is equivalent to

$$\frac{\mathrm{d}\bar{T}}{\mathrm{d}t} = \frac{\alpha}{kl}\left(q_0(t) - q_l(t)\right).$$

Given the heat fluxes in equation (1), the spatial average temperature satisfies

$$\begin{aligned}\frac{\mathrm{d}\bar{T}}{\mathrm{d}t} = \frac{\alpha}{kl}\big(&h_0(T_0 - T(0,t)) \\ &+ \tilde{q}_0 - h_l(T(l,t) - T_l) - \tilde{q}_l\big).\end{aligned} \tag{4}$$

Equation (4) follows directly from the heat equation and boundary conditions, but cannot be solved in general without first solving the heat equation for the unknown surface temperatures $T(0,t)$ and $T(l,t)$. However, under the lumped capacitance approximation

$$\boxed{T(0,t) \approx \bar{T}(t) \approx T(l,t) \text{ for all } t > 0,} \tag{5}$$

equation (4) reduces to

$$\frac{\mathrm{d}\bar{T}}{\mathrm{d}t} \approx -\frac{\alpha(h_0+h_l)}{kl}(\bar{T}(t)-T_{\mathrm{ref}}).$$

Given the initial condition $T(x,0)=T_i$ for all $x \in [0,l]$, the solution is $\bar{T}(t) \approx T^{\mathrm{LC}}(t)$, where

$$T^{\mathrm{LC}}(t) \equiv T_{\mathrm{ref}} + (T_i - T_{\mathrm{ref}})e^{-t/t_c} \tag{6}$$

is the lumped capacitance approximation to the temperature distribution, with time constant

$$t_c \equiv \frac{kl}{\alpha(h_0+h_l)}.$$

The reference temperatures is

$$T_{\mathrm{ref}} \equiv \frac{h_0 T_0 + \tilde{q}_0 + h_l T_l - \tilde{q}_l}{h_0+h_l}.$$

2.3. Error metrics

In [22], Alhama and Campo use an error metric equivalent to

$$\gamma_{\mathrm{AC}}(t) \equiv \frac{T_{\max}(t) - \min\{T(0,t), T(l,t)\}}{T_{\max}(t) - T_{\mathrm{ref}}},$$

where $T_{\max}(t) = \sup\{T(x,t) \mid x \in [0,l]\}$. This metric poses three difficulties. First, it may grow without bound as $T_{\max}(t) \to T_{\mathrm{ref}}$. If the lumped capacitance approximation is accurate, this is exactly the limiting behavior as $t \to \infty$, so we can only reasonably expect γ_{AC} to be small for small t. Second, γ_{AC} is rather far removed from physical quantities of interest, such as surface heat fluxes and stored energy. Third, γ_{AC} only indirectly reflects the basic lumped capacitance assumption (5), which states that the surface temperatures are nearly equal to the average temperature, rather than the maximum temperature used in γ_{AC}.

To address these issues, we propose three new error metrics. The first two,

$$\begin{aligned} \gamma_0(t) &\equiv \left|\frac{T(0,t)-T^{\mathrm{LC}}(t)}{T_i - T_{\mathrm{ref}}}\right| \\ \gamma_l(t) &\equiv \left|\frac{T(l,t)-T^{\mathrm{LC}}(t)}{T_i - T_{\mathrm{ref}}}\right|, \end{aligned} \tag{7}$$

directly quantify the accuracy of the fundamental lumped capacitance assumption (5). They are also relevant to applications, since the surface temperatures determine the surface heat fluxes and hence the net heat flow through the slab. The third error metric,

$$\bar{\gamma}(t) \equiv \left|\frac{\bar{T}(t)-T^{\mathrm{LC}}(t)}{T_i - T_{\mathrm{ref}}}\right|, \tag{8}$$

quantifies the accuracy in approximating the spatial average temperature. This is of interest in thermal storage applications, where the heat fluxes across the boundary are less important than the internal energy.

In definitions (7) and (8), we have normalized by $T_i - T_{\mathrm{ref}}$, which (if the lumped capacitance approximation is accurate) is the maximum deviation from the equilibrium temperature T_{ref}. The denominator is zero only in the trivial case where $T_i = T_{\mathrm{ref}}$, meaning the system starts and remains in equilibrium. In this case, the lumped capacitance approximation is exact for all time.

2.4. Analytical solution

To simplify analysis, we introduce the dimensionless space and time variables $\xi \equiv x/l$ and $\tau \equiv \alpha t/l^2$, and the dimensionless temperatures

$$\begin{aligned} \theta(\xi,\tau) &\equiv \frac{T(x,t)-T_{\mathrm{ref}}}{T_i - T_{\mathrm{ref}}} \\ \theta_0 &\equiv \frac{T_0 + \tilde{q}_0/h_0 - T_{\mathrm{ref}}}{T_i - T_{\mathrm{ref}}} \\ \theta_l &\equiv \frac{T_l - \tilde{q}_l/h_l - T_{\mathrm{ref}}}{T_i - T_{\mathrm{ref}}}. \end{aligned}$$

Under these transformations, the lumped capacitance approximation to the dimensionless temperature distribution is $\bar{\theta}(\tau) \approx \theta^{\mathrm{LC}}(\tau) \equiv e^{-\tau/\tau_c}$, where $\bar{\theta}(\tau) \equiv \int_0^1 \theta(\xi,\tau)\mathrm{d}\xi$ is the spatial average dimensionless temperature and $\tau_c \equiv 1/(\mathrm{Bi}_0 + \mathrm{Bi}_l)$ is the dimensionless time constant. The surface temperature approximation errors from equation (7) reduce to

$$\begin{aligned} \gamma_0(t) &= \left|\theta(0,\tau) - \theta^{\mathrm{LC}}(\tau)\right| \\ \gamma_l(t) &= \left|\theta(1,\tau) - \theta^{\mathrm{LC}}(\tau)\right|. \end{aligned} \tag{9}$$

The spatial average temperature error is

$$\bar{\gamma}(t) = \left|\bar{\theta}(\tau) - \theta^{\mathrm{LC}}(\tau)\right|. \tag{10}$$

In dimensionless form, problem 2 becomes

$$\begin{aligned}
&\frac{\partial\theta}{\partial\tau} = \frac{\partial^2\theta}{\partial\xi^2}, \quad \xi\in[0,1],\ \tau\geq 0\\
&\theta(\xi,0) = 1, \quad \xi\in[0,1]\\
&\left.\frac{\partial\theta}{\partial\xi}\right|_{0,\tau} = -\mathrm{Bi}_0(\theta_0-\theta(0,\tau)), \quad \tau\geq 0\\
&\left.\frac{\partial\theta}{\partial\xi}\right|_{1,\tau} = -\mathrm{Bi}_l(\theta(1,\tau)-\theta_l), \quad \tau\geq 0.
\end{aligned} \tag{11}$$

Applying separation of variables and Sturm-Liouville theory to problem (11) (see Appendix A) gives the solution

$$\theta(\xi,\tau) = \phi(\xi) + \sum_{n=1}^{\infty} A_n e^{-\omega_n^2\tau} X_n(\xi).$$

The steady state component is $\phi(\xi) = a\xi + b$, with $a = \mathrm{Bi}_0(b-\theta_0)$ and $b = \theta_0/(1+1/\mathrm{Bi}_0+1/\mathrm{Bi}_l)$. The n^{th} eigenfunction of the transient component is $X_n(\xi) = \cos(\omega_n\xi) + (\mathrm{Bi}_0/\omega_n)\sin(\omega_n\xi)$, with eigenvalue ω_n solving the transcendental equation $\cot(\omega) = (\omega - \mathrm{Bi}_0\mathrm{Bi}_l/\omega)/(\mathrm{Bi}_0+\mathrm{Bi}_l)$. The n^{th} coefficient is

$$A_n = \frac{2\omega_n\sin(\omega_n)(\mathrm{Bi}_0+\mathrm{Bi}_l)}{\omega_n^2[\mathrm{Bi}_0+\mathrm{Bi}_l-\sin^2(\omega_n)]+\mathrm{Bi}_0\mathrm{Bi}_l\sin^2(\omega_n)}. \tag{12}$$

3. Results

The following results are for the initial condition shown in Figure 2, where

$$T_i = T_0+\tilde{q}_0/h_0 \quad\Longrightarrow\quad \theta_0 = 1 \text{ and } \theta_l = -\mathrm{Bi}_0/\mathrm{Bi}_l.$$

Physically, this models a uniform slab initially in thermal equilibrium with identical environments at either boundary. Both surfaces of the slab initially receive the temperature-independent heat flux $\tilde{q}_0$, and lose an equal heat flux to the environment due to convection or radiation. At $t=0$, the driving temperature to the right of the slab suddenly changes from T_0 to T_l, the heat transfer coefficient changes from h_0 to h_l, and the temperature-independent heat flux changes from $\tilde{q}_0$ to $\tilde{q}_l$.

3.1. Steady state accuracy

For large times, the accuracy of the lumped capacitance approximation can be analyzed in terms of $\phi(\xi)$ only, since $\lim_{\tau\to\infty}\theta(\xi,\tau) = \phi(\xi)$. Noting that $\theta^{\mathrm{LC}}(\tau)\to 0$ as $\tau\to\infty$, the steady state surface temperature approximation errors are

$$\begin{aligned}
\gamma_0^{\mathrm{SS}} &\equiv \lim_{t\to\infty}\gamma_0(t) = |\phi(0)| = \frac{1}{1+1/\mathrm{Bi}_0+1/\mathrm{Bi}_l}\\
\gamma_l^{\mathrm{SS}} &\equiv \lim_{t\to\infty}\gamma_l(t) = |\phi(1)| = \frac{\mathrm{Bi}_0/\mathrm{Bi}_l}{1+1/\mathrm{Bi}_0+1/\mathrm{Bi}_l}.
\end{aligned}$$

Similarly, since the spatial average temperature in steady state is

$$\bar{\theta}^{\mathrm{SS}} = \lim_{\tau\to\infty}\bar{\theta}(\tau) = \int_0^1 \phi(\xi)\mathrm{d}\xi,$$

the spatial average temperature approximation error reduces to

$$\bar{\gamma}^{\mathrm{SS}} \equiv \lim_{t\to\infty}\bar{\gamma}(t) = \frac{|1-\mathrm{Bi}_0/\mathrm{Bi}_l|}{2(1+1/\mathrm{Bi}_0+1/\mathrm{Bi}_l)}. \tag{13}$$

An immediate consequence of equation (13) is that $\bar{\gamma}^{\mathrm{SS}} = 0$ whenever $\mathrm{Bi}_0 = \mathrm{Bi}_l \neq 0$, no matter how large the Biot numbers are. In other words, once the slab reaches steady state, the lumped capacitance approximation is nearly exact whenever the Biot numbers are nearly equal. In §3.2, we shall see a similar pattern in the slab's transient response. Figure 3 shows contours of the approximation errors for $\mathrm{Bi}_0, \mathrm{Bi}_l \in [0,1]$. Interestingly, γ_l^{SS} and $\bar{\gamma}^{\mathrm{SS}}$ are more sensitive to Bi_0 than Bi_l. This asymmetry is not reflected in previous results.

3.2. Transient accuracy

To quantify the approximation accuracy for small times, we compare the lumped solution to the first N terms of $\theta(\xi,\tau)$, with N chosen such that $|A_n|\ e^{-\omega_n^2\beta\tau_c}\ \|X_n(\xi)\|_\infty \leq 10^{-5}$ for all $n > N$. We compute the analytical solution for 450,000 combinations of the parameters Bi_0, Bi_l, and β. We consider 300 values each of Bi_0 and Bi_l, linearly spaced in $[0,1]$. The dimensionless times considered are $\tau = \beta\tau_c$, with $\beta\in\{0.05, 0.35, 0.8, 1.6\}$, as well as steady state ($\beta\to\infty$). These times correspond to the temperature difference $T^{\mathrm{LC}}(t) - T_{\mathrm{ref}}$ decaying to about 95, 70, 45, 20, and 0% of the initial difference $T_i - T_{\mathrm{ref}}$, respectively. The spatial average temperature $\bar{\theta}(\tau)$ and the lumped capacitance approximation $\theta^{\mathrm{LC}}(\tau)$ were also computed at each parameter combination, and used to find the errors $\gamma_0(t)$, $\gamma_l(t)$, and $\bar{\gamma}(t)$. Figure 4 shows contours of each error metric at each value of β.

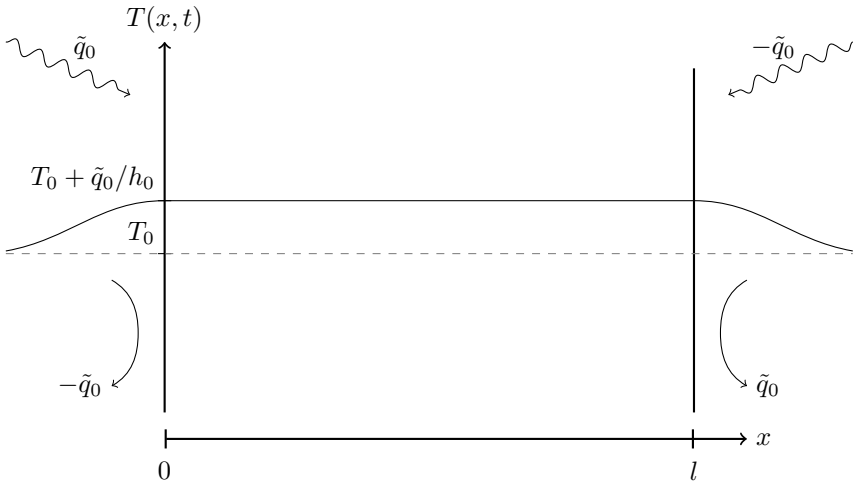

Figure 2: initial state of the slab.

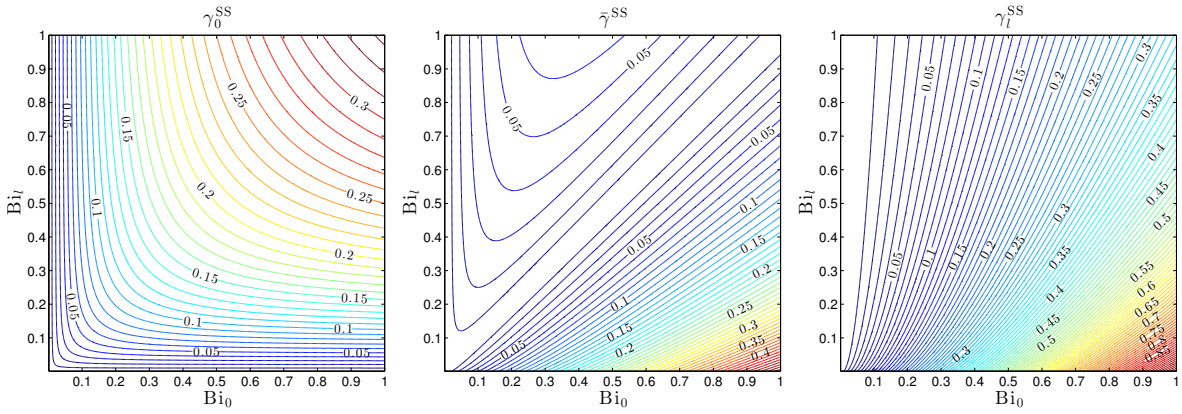

Figure 3: steady state errors with contours at intervals of 0.01. The left-hand surface temperature error γ_0^{SS} is small when either Bi_0 or Bi_l is small. The right-hand surface temperature error γ_l^{SS} is sensitive to Bi_0, but actually decreases as Bi_l grows. The spatial average temperature error $\bar{\gamma}^{\mathrm{SS}}$ is zero along the line $\mathrm{Bi}_0 = \mathrm{Bi}_l$.

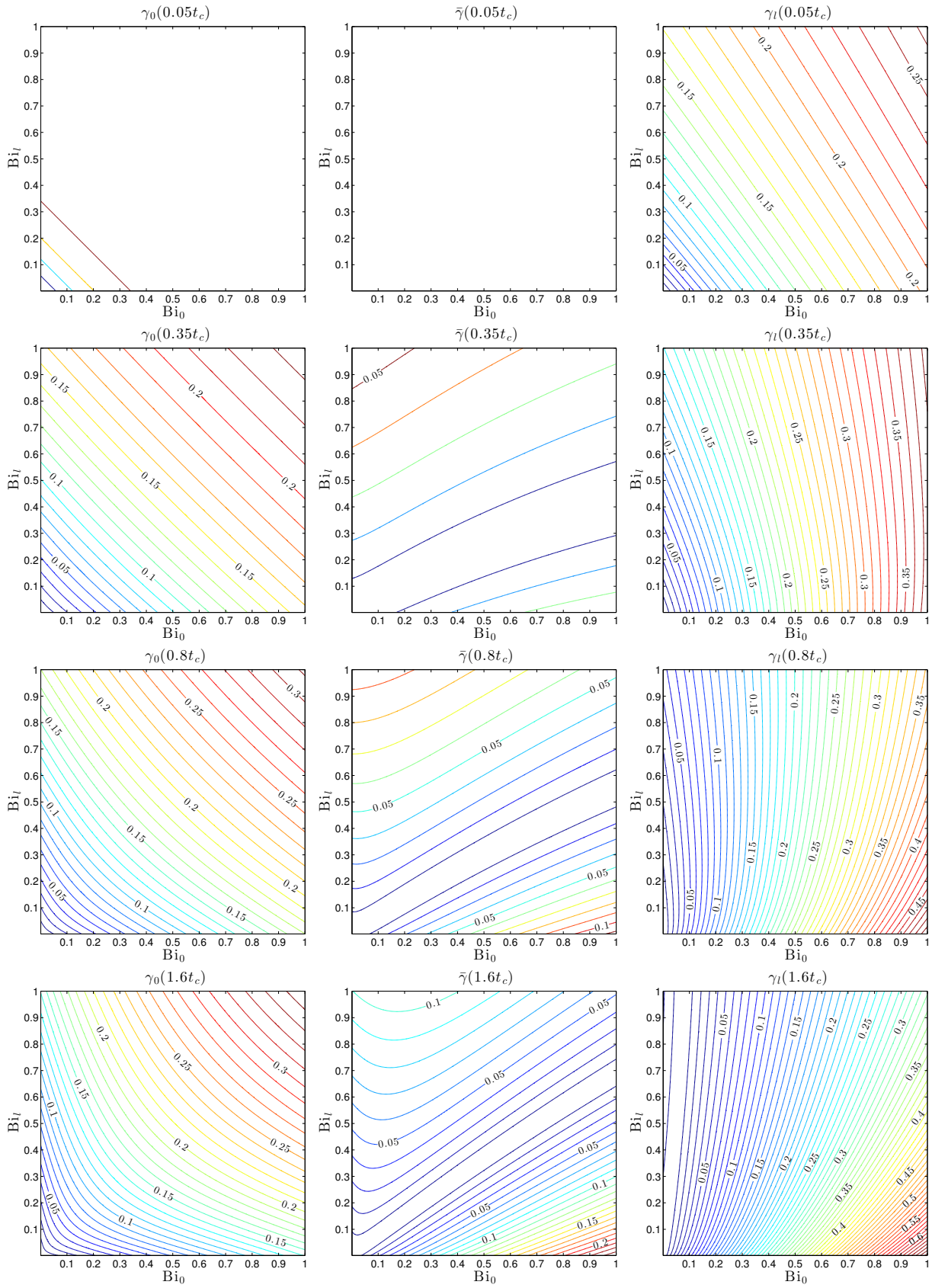

Figure 4: contour plots of the errors $\gamma_0(\beta t_c)$ (left), $\bar{\gamma}(\beta t_c)$ (center), and $\gamma_l(\beta t_c)$ (right). Contours are at intervals of 0.01. The top row ($\beta = 0.05$) shows the early transient errors. As time increases, the errors approach the steady-state errors in Figure 3.

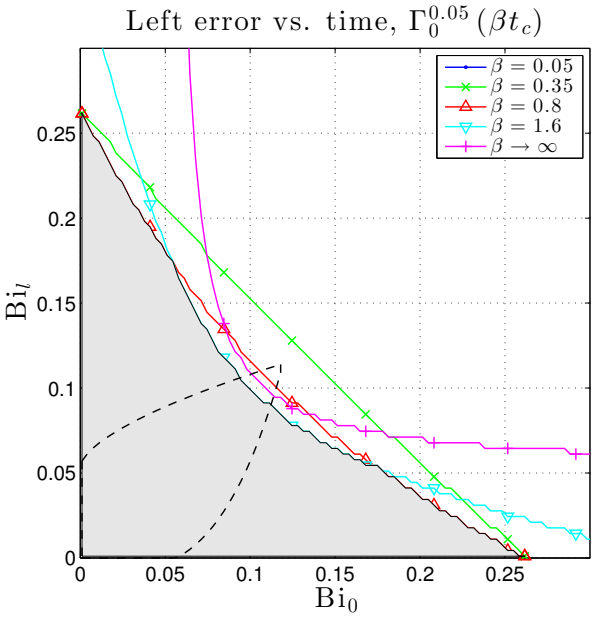

Figure 5: the Biot pairs that maintain the left-hand surface temperature error $\gamma_0(t)$ under 5% at each multiple β of the time constant t_c. The shaded set is their intersection, $\Gamma_0^{0.05}$. The dashed curve is the boundary of $\Gamma_{\mathrm{AC}}^{0.05}$, the 5% error set from [22].

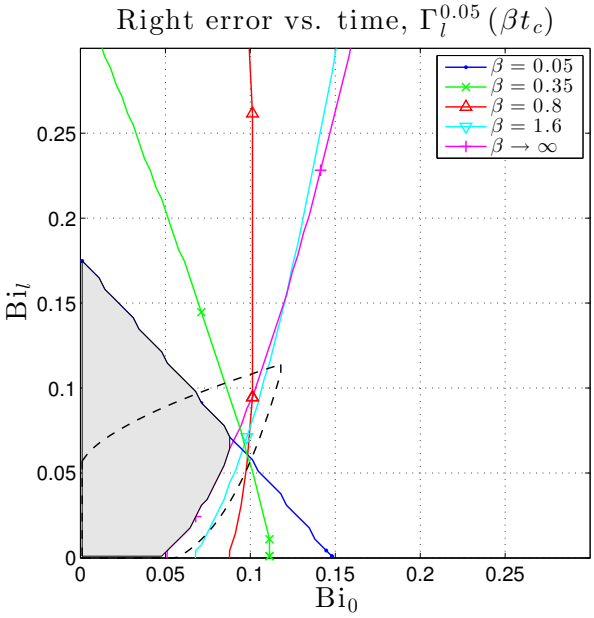

Figure 6: the Biot pairs that maintain the right-hand surface temperature error $\gamma_l(t)$ under 5% at each $t = \beta t_c$. The shaded set $\Gamma_l^{0.05}$ is similar in area to $\Gamma_{\mathrm{AC}}^{0.05}$ (dashed curve), but more restrictive on Bi_0 and less restrictive on Bi_l.

3.2.1. Surface temperature errors

The left-hand column of Figure 4 shows the level sets of $\gamma_0(t)$ for each $t = \beta t_c$. For very small times, the errors are small for a wide range of Biot numbers. As t increases, however, the errors grow quickly. The errors are nearly symmetric in Bi_0 and Bi_l. The sets of Biot numbers that maintain $\gamma_0(t)$ below the threshold δ at a particular t,

$$\Gamma_0^\delta(t) \equiv \{\mathrm{Bi}_0, \mathrm{Bi}_l \geq 0 \mid \gamma_0(t) \leq \delta\},$$

are shown in Figure 5 for $\delta = 0.05$. The shaded area is their intersection,

$$\Gamma_0^\delta \equiv \bigcap_{t \geq 0} \Gamma_0^\delta(t).$$

The right-hand column of Figure 4 shows the level sets of $\gamma_l(t)$ for each $t = \beta t_c$. The errors are initially large and nearly symmetric in the Biot numbers. As t increases, the errors for large Bi_0 increase, while for large Bi_l they decrease. For times above about one time constant, the lumped capacitance approximation to $T(l,t)$ actually improves with increasing Bi_l. These phenomena are also demonstrated in Figure 6, which shows the sets

$$\Gamma_l^\delta(t) \equiv \{\mathrm{Bi}_0, \mathrm{Bi}_l \geq 0 \mid \gamma_l(t) \leq \delta\}$$

and

$$\Gamma_l^\delta \equiv \bigcap_{t \geq 0} \Gamma_l^\delta(t)$$

for $\delta = 0.05$.

3.2.2. Spatial average temperature error

The center column of Figure 4 shows the errors in approximating $\bar{T}(t)$. The approximation is nearly exact for all $\mathrm{Bi}_0, \mathrm{Bi}_l \leq 1$ and times less than about one time constant. For $t > t_c$, $\bar{\gamma}(t)$ remains small if Bi_0 and Bi_l are sufficiently close to the line $\mathrm{Bi}_l = m(t)\mathrm{Bi}_0$, where the slope $m(t)$ approaches 1 from below as $t \to \infty$. The reason for this accuracy is the fact that $T^{\mathrm{LC}}(t)$ underestimates temperatures near $x = 0$ and overestimates those near $x = l$. When the temperature is averaged over space, these errors tend to cancel out. Thus, if one is only interested in $\bar{T}(t)$, for instance in thermal storage applications, then a wide range of Biot numbers are acceptable. This fact is also demonstrated by the shaded area in Figure 7, which shows the sets

$$\bar{\Gamma}^\delta(t) \equiv \{\mathrm{Bi}_0, \mathrm{Bi}_l \geq 0 \mid \bar{\gamma}(t) \leq \delta\}$$

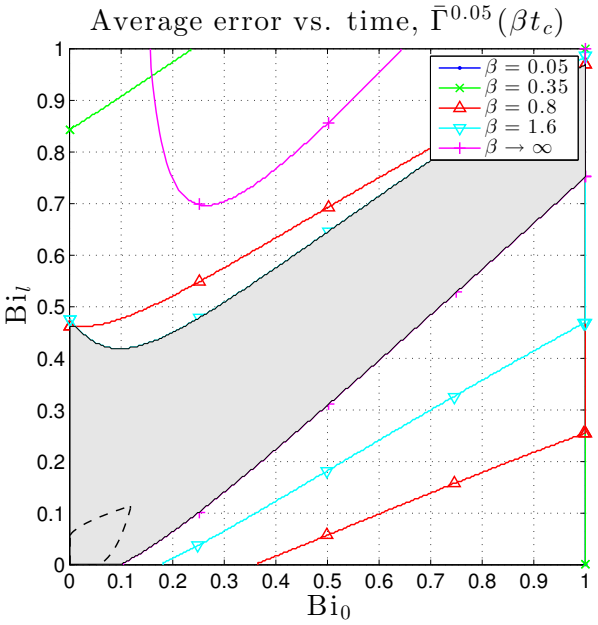

Figure 7: the Biot pairs that maintain the spatial average temperature error $\bar{\gamma}(t)$ under 5% at each $t = \beta t_c$. The shaded area is their intersection, $\bar{\Gamma}^{0.05}$. For $\beta \leq 0.35$, any Biot pair with $\mathrm{Bi}_0, \mathrm{Bi}_l \leq 1$ is acceptable.

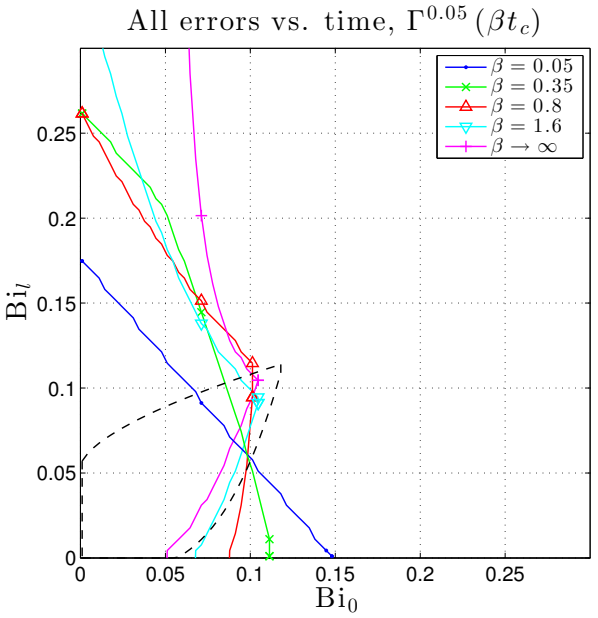

Figure 8: the Biot pairs that maintain all errors under 5%, for each $t = \beta t_c$. As time increases, the bound on Bi_0 tightens while the bound on Bi_l loosens.

and

$$\bar{\Gamma}^{\delta} \equiv \bigcap_{t \geq 0} \bar{\Gamma}^{\delta}(t)$$

for $\delta = 0.05$.

3.2.3. *All errors*

We now consider the sets of Biot numbers for which all error metrics are maintained below a threshold δ. Figure 8 shows how the acceptable Biot numbers change with time. The sets pictured are

$$\Gamma^{0.05}(t) \equiv \Gamma_0^{0.05}(t) \cap \Gamma_l^{0.05}(t) \cap \bar{\Gamma}^{0.05}(t)$$

for $t = \beta t_c$, with $\beta \in \{0.05, 0.35, 0.8, 1.6\}$ and $\beta \to \infty$. As expected, these sets shrink as time increases. The sets look similar to those shown in Figure 6, since for most Bi_0, Bi_l, and β, $\gamma_l(\beta t_c) > \max(\gamma_0(\beta t_c), \bar{\gamma}(\beta t_c))$. For large t, however, $\gamma_0(t)$ exceeds $\gamma_l(t)$, which restricts the values in the upper left of the plot.

Figure 9 shows the sets

$$\Gamma^{\delta} \equiv \Gamma_0^{\delta} \cap \Gamma_l^{\delta} \cap \bar{\Gamma}^{\delta}$$

for $\delta \in \{0.05, 0.1, \ldots, 0.35\}$. These sets contain the Biot numbers for which all error metrics are less than δ for all time. As expected, the sets grow in area as the error threshold increases.

We can approximate the set Γ^{δ} for a given δ by fitting curves to the upper and lower boundaries shown in Figure 9. This gives

$$\Gamma^{\delta} \approx \{\mathrm{Bi}_0, \mathrm{Bi}_l \geq 0 \mid f_{1\delta}(\mathrm{Bi}_0) \leq \mathrm{Bi}_l \leq f_{2\delta}(\mathrm{Bi}_0)\} \tag{14}$$

where $f_{i\delta}(\mathrm{Bi}_0) = (a_{i\delta} + b_{i\delta}\mathrm{Bi}_0)^{c_{i\delta}}$. Table 1 gives the coefficients $a_{i\delta}$, $b_{i\delta}$, and $c_{i\delta}$ for $i \in \{1, 2\}$ and $\delta \in \{0.05, 0.1, \ldots, 0.35\}$. The coefficients were fit using the Box-Cox transformation and linear regression.

3.3. *Examples*

In this section, we apply the results in §3 to examples involving a wall and a window. The first example demonstrates that a uniform wall may be lumped with fair accuracy, assuming the outdoor conditions are mild. The second example demonstrates that a single-pane window may be lumped under a wide range of conditions.

3.3.1. *Wind over a wall*

In this example, we consider a single-layer wall of thickness $l = 0.1$ m, thermal conductivity $k = 0.3$ W/m·K, and thermal diffusivity $\alpha = 5 \times 10^{-7}$ m^2/s,

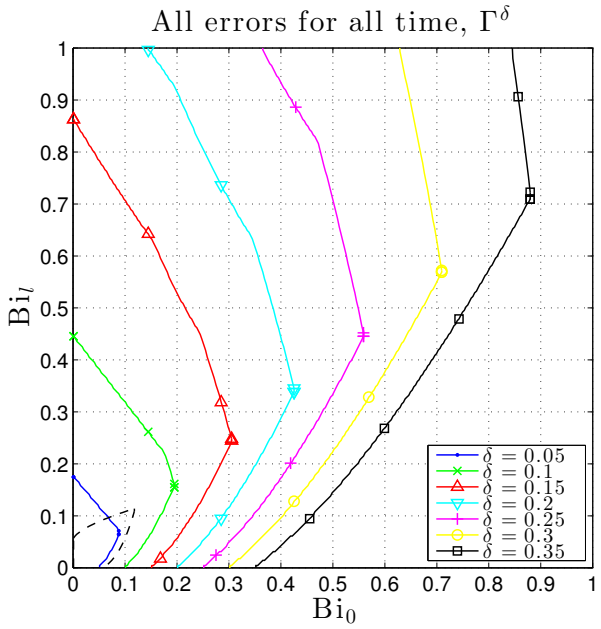

Figure 9: the Biot pairs that maintain all errors under δ for all time. The sets are shown for error thresholds δ between 5 and 35%.

Table 1: coefficients of the curves $f_{1\delta}$ and $f_{2\delta}$ bounding the sets Γ^δ in Figure 9.

δ	$a_{1\delta}$	$b_{1\delta}$	$c_{1\delta}$	$a_{2\delta}$	$b_{2\delta}$	$c_{2\delta}$
0.05	-0.18	5.70	2.41	0.27	-1.49	1.31
0.1	-0.27	3.36	1.92	0.40	-1.30	0.89
0.15	-0.32	2.63	1.87	0.83	-2.11	0.72
0.2	-0.35	2.16	1.86	1.42	-2.73	0.68
0.25	-0.36	1.83	1.85	2.62	-4.40	0.41
0.3	-0.36	1.58	1.83	4.51	-5.58	0.91
0.35	-0.36	1.39	1.82	8.49	-8.88	0.84

separating a room ($x < 0$) from the outdoors ($x > l$). Initially, the wall is at the uniform temperature $T_0 = 293$ K with film coefficient $h_0 = 1$ W/m^2·K at both surfaces. At $t = 0$, a cool wind suddenly changes the outdoor temperature to $T_l = 289$ K and film coefficient to $h_l = 3$ W/m^2·K, while the indoor environment remains constant. We assume that $\tilde{q}_0 = \tilde{q}_l = 0$, and wish to estimate the accuracy of the lumped capacitance approximations to $T(0,t)$ and $T(l,t)$ after 15 and 90 minutes.

The Biot numbers are $\mathrm{Bi}_0 = h_0 l/k = 0.33$ and $\mathrm{Bi}_l = h_l l/k = 1$. The dimensionless time constant is $\tau_c = 1/(\mathrm{Bi}_0 + \mathrm{Bi}_l) = 0.75$, giving a time constant $t_c = l^2\tau_c/\alpha = 15{,}000$ s, or about 4 hours and 10 minutes. The times of interest are $t_1 = \beta_1 t_c = 900$ s, and $t_2 = \beta_2 t_c = 5{,}400$ s, so $\beta_1 = 0.06$ and $\beta_2 = 0.36$. From the top two plots in the left column of Figure 4, the approximation errors at t_1 and t_2 are about $\gamma_0(\beta_1 t_c) = 0.05$ and $\gamma_0(\beta_2 t_c) = 0.2$. Similarly, from the top two plots in the right column, $\gamma_l(\beta_1 t_c) = 0.2$ and $\beta_l(\beta_2 t_c) = 0.22$. The reference temperatures is $T_{\mathrm{ref}} = 290$ K, so the temperature approximation errors are

$$\begin{aligned}
\left|T(0,t_1) - T^{\mathrm{LC}}(t_1)\right| &= \gamma_0(t_1)(T_0 - T_{\mathrm{ref}}) = 0.15 \text{ K} \\
\left|T(l,t_1) - T^{\mathrm{LC}}(t_1)\right| &= \gamma_l(t_1)(T_0 - T_{\mathrm{ref}}) = 0.6 \text{ K} \\
\left|T(0,t_2) - T^{\mathrm{LC}}(t_2)\right| &= \gamma_0(t_2)(T_0 - T_{\mathrm{ref}}) = 0.6 \text{ K} \\
\left|T(l,t_2) - T^{\mathrm{LC}}(t_2)\right| &= \gamma_l(t_2)(T_0 - T_{\mathrm{ref}}) = 0.66 \text{ K}.
\end{aligned}$$

Note that even though the Biot numbers in this problem are large, the temperature approximation errors are well below 1 K, the measurement uncertainty of a typical thermocouple.

3.3.2. Accuracy regime for a window

For a second example, we consider a single-pane window of thickness $l = 0.005$ m and thermal conductivity $k = 1$ W/m·K, separating a room ($x < 0$) from the outdoors ($x > l$). The window is initially at temperature $T_0 + \tilde{q}_0/h_0$, with heat transfer coefficient h_0 and temperature-independent heat gain $\tilde{q}_0$ at both surfaces. At $t = 0$, the outdoor environment suddenly changes to $T_l \neq T_0$, $h_l \neq h_0$, and $\tilde{q}_l \neq \tilde{q}_0$. We wish to find the largest h_l such that the lumped capacitance approximation is accurate to within 5% error by all metrics, for all time, and for all $h_0 \leq 10$ W/m^2·K.

The room-side Biot number satisfies $\mathrm{Bi}_0 = h_0 l/k \leq 0.05$. From Figure 9, the tightest bound on Bi_l occurs at $\mathrm{Bi}_0 = 0.05$. From equation (14) and Table 1,

the largest Bi_l such that $(\mathrm{Bi}_0, \mathrm{Bi}_l) \in \Gamma^{0.05}$ satisfies

$$\mathrm{Bi}_l^{\max} = f_{2,0.05}(0.05) = [0.27-1.49(0.05)]^{1.31} = 0.12.$$

Thus, all error metrics are under 5% whenever $h_l \leq \mathrm{Bi}_l^{\max} k/l = 23.6$ W/m^2·K. This encompasses any situation one might practically encounter in a building.

4. Conclusion

In this paper, we studied conduction through a slab subject to an asymmetric step change of boundary conditions. We compared the lumped capacitance approximation to the analytical solution for 450,000 parameter values, with Biot numbers between zero and one, and times ranging from early transients through steady state. We defined three new error metrics intended to

1. assess the validity of the fundamental assumption (5), and
2. quantify the accuracy of approximating the surface temperatures and spatial average temperature, which in turn determine the surface fluxes and internal energy.

We provided numerical expressions for the sets of Biot numbers that maintain all error metrics below 5, 10, ..., and 35% for all time.

We showed that, depending on the physical quantities of interest, Biot numbers well beyond the conventional upper bound of 0.1 may be acceptable. In particular, if one is only interested in the internal energy of the slab, then Biot numbers of 1 or more maintain the error under 5% at all times, provided that they are close to the line $\mathrm{Bi}_l = \mathrm{Bi}_0$.

We also showed that the strongest influence on the surface temperature errors is Bi_0, the Biot number at the surface of the slab that does *not* experience a step change in environmental conditions. This may explain the surprising accuracy of RC networks in buildings, where indoor conditions are maintained nearly constant, while outdoor air temperatures, film coefficients, and solar gains can change rapidly in response to wind and clouds. The indoor heat transfer coefficient h_0, which typically models mild natural convection, is often small. Thus, $\mathrm{Bi}_0 = h_0 l/k$ is also often small, and the surface temperature approximations may be accurate for a wide range of outdoor conditions.

It would be interesting to extend this work to multilayer slabs, which model a larger set of walls and windows. This is technically possible given the recently published analytical solutions for multilayer slabs [23], but it may be complicated by the new parameters introduced by each layer. The accuracy of higher-order RC network models of the slab, or of refined lumped approximations based on Hermite integral approximations [24] or perturbation methods [25], could also be analyzed.

Finally, we highlight cases where an RC network may be a poor predictor of indoor air temperatures. Errors may arise from lumped capacitance approximations to walls that are thick and well-insulated. Walls that have large convection coefficients at the indoor surface, *e.g.*, due to mechanical systems forcing air over them, will likely have large Bi_0 and poor lumped capacitance accuracy. Failures could also occur in the presence of significant radiative coupling between walls, or of film coefficients that depend strongly on the driving temperature gradients. Parameters estimated from data with low information content may also lead to poor predictions. Although care should be taken in these cases, the results in this paper lend theoretical support to RC network building models.

Acknowledgements

The authors gratefully acknowledge support from the Hydro Research Foundation Fellowship and the Energy Efficiency and Renewable Energy Program of the U.S. Department of Energy.

References

[1] Buildings energy databook, chapter 1: Buildings sector., Tech. rep., Office of Energy Efficiency and Renewable Energy, US Department of Energy (2011).

[2] Commercial Buildings Energy Consumption Survey, Table E1A: Major Fuel Consumption (BTU) by End Use for All Buildings., Tech. rep., Energy Information Administration, U.S. Department of Energy (2003).

[3] Residential Energy Consumption Survey, Table CE3.1: End-Use Consumption Totals and Averages, U.S. Homes., Tech. rep., Energy Information Administration, U.S. Department of Energy (2009).

[4] Energy Impact of Commercial Building Controls and Performance Diagnostics: Market Characterization, Energy Impact of Building Faults and the Energy Savings Potential., Tech. Rep. D0180, TIAX (2005).

[5] J. Lee, Model Predictice Control: Review of the Three Decades of Development., International Journal of Control, Automation and Systems 9 (3) (2011) 414–424.

[6] J. Siroky, F. Oldewurtel, J. Cigler, S. Privara, Experimental Analysis of Model Predictive Control for an Energy Efficient Building Heating system., Applied Energy 88 (2011) 3079–3087.
[7] D. Sturzenegger, D. Gyalistras, M. Gwerder, C. Sagerschnig, M. Morari, R. Smith, Model Predictive Control of a Swiss Office Building, in: 11th RHEVA World Congress Clima, 2013.
[8] S. Bengea, A. Kelman, F. Borrelli, R. Taylor, S. Narayanan, Model Predictive Control for Mid-size Commercial Building HVAC: Implementation, Results and Energy Savings., in: International Conference on Building Energy and Environment, 2012.
[9] A. Afram, F. Janabi-Sharifi, Theory and applications of HVAC control systems – A review of model predictive control (MPC), Building and Environment 72 (2014) 343–355.
[10] S. Privara, J. Cigler, Z. Vana, F. Oldewurtel, C. Sagerschnig, Building modeling as a crucial part for building predictive control., Energy and Buildings 56 (2013) 8–22.
[11] R. Kramer, J. van Schijndel, H. Schellen, Simplified thermal and hygric building models: a literature review., Frontiers of Architectural Research 1 (4) (2012) 318–325.
[12] P. Radecki, B. Hencey, Online building thermal parameter estimation via unscented Kalman filtering, in: American Control Conference, 2012, pp. 3056–3062.
[13] P. Radecki, B. Hencey, Online thermal estimation, control, and self-excitation of buildings, in: Conference on Decision and Control, IEEE, 2013, pp. 4802–4807.
[14] Y. Lin, T. Middelkoop, P. Barooah, Issues in identification of control-oriented thermal models of zones in multizone buildings, in: Conference on Decision and Control, IEEE, 2012.
[15] J. Dobbs, B. Hencey, Model Predictive HVAC Control with Online Occupancy Model, Energy and Buildings 82 (2014) 675–684.
[16] F. Oldewurtel, A. Parisio, C. Jones, D. Gyalistras, M. Gwerder, V. Stauch, B. Lehmann, M. Morari, Use of model predictive control and weather forecasts for energy efficient building climate control, Energy and Buildings 45 (2012) 15–27.
[17] M. Maasoumy, Controlling energy-efficient buildings in the context of smart grid: A cyber physical system approach, Ph.D. thesis, University of California, Berkeley (2013).
[18] US Department of Energy, EnergyPlus Engineering Reference. (2014).
[19] J. H. Lienhard IV, J. H. Lienhard V, A Heat Transfer Textbook, 4th Edition, Phlogiston Press, 2012.
[20] D. Poulikakos, Conduction Heat Transfer, Prentice-Hall, 1994.
[21] H. Baehr, K. Stephan, Heat and Mass Transfer, 2nd Edition, Springer, 2006.
[22] F. Alhama, A. Campo, The connection between the distributed and lumped models for asymmetric cooling of long slabs by heat convection, International Communications in Heat and Mass Transfer 28 (1) (2001) 127–137.
[23] R. I. Hickson, S. I. Barry, G. N. Mercer, Critical times in multilyaer diffusion. part 1: Exact solutions, International Journal of Heat and Mass Transfer 52 (2009) 5776–5783.
[24] J. Su, Improved lumped models for asymmetric cooling of a long slab by heat convection, International Communications in Heat and Mass Transfer 28 (7) (2001) 973–983.
[25] H. Sadat, A general lumped model for transient heat conduction in one-dimensional geometries, Applied Thermal Engineering 25 (4) (2005) 567–576.
[26] H. Carslaw, J. Jaeger, Conduction of Heat in Solids, Clarendon Press, 1959.

Appendix A. Analytical solution details

In this appendix, we solve the dimensionless problem (11) by separation of variables. This solution is not new (see, for example, [26]), but provides some insight into the problem. Due to the nonhomogeneous boundary conditions, we look for a solution of the form $\theta(\xi,\tau) = \phi(\xi) + \psi(\xi,\tau)$, where $\psi(\xi,\tau) = f(\xi)g(\tau)$. In terms of $\psi(\xi,\tau)$ and $\phi(\xi)$, problem (11) is

$$\begin{aligned}
&\frac{\partial\psi}{\partial\tau} = \frac{\partial^2\psi}{\partial\xi^2} + \frac{\mathrm{d}^2\phi}{\mathrm{d}\xi^2}, \quad \xi\in[0,1],\ \tau\geq 0\\
&\phi(\xi)+\psi(\xi,0) = 1, \quad \xi\in[0,1]\\
&\left.\frac{\partial\psi}{\partial\xi}\right|_{0,\tau} + \left.\frac{\mathrm{d}\phi}{\mathrm{d}\xi}\right|_0 = -\mathrm{Bi}_0\left(\theta_0-\psi(0,\tau)-\phi(0)\right),\ \tau\geq 0\\
&\left.\frac{\partial\psi}{\partial\xi}\right|_{1,\tau} + \left.\frac{\mathrm{d}\phi}{\mathrm{d}\xi}\right|_1 = -\mathrm{Bi}_l\left(\psi(1,\tau)+\phi(1)-\theta_l\right),\ \tau\geq 0,
\end{aligned}$$

which we divide into a subproblem in $\psi(\xi,\tau)$ and a subproblem in $\phi(\xi)$, coupled by the initial condition. We choose the $\phi(\xi)$ subproblem to be steady state, and include the nonhomogeneous parts of the boundary conditions in it. This gives the subproblems

$$\begin{aligned}
&\frac{\mathrm{d}^2\phi}{\mathrm{d}\xi^2} = 0, \quad \xi\in[0,1]\\
&\left.\frac{\mathrm{d}\phi}{\mathrm{d}\xi}\right|_0 = -\mathrm{Bi}_0\left(\theta_0-\phi(0)\right)\\
&\left.\frac{\mathrm{d}\phi}{\mathrm{d}\xi}\right|_1 = -\mathrm{Bi}_l\left(\phi(1)-\theta_l\right)
\end{aligned} \tag{A.1}$$

and

$$\begin{aligned}
&\frac{\partial\psi}{\partial\tau} = \frac{\partial^2\psi}{\partial\xi^2}, \quad \xi\in[0,1],\ \tau\geq 0\\
&\left.\frac{\partial\psi}{\partial\xi}\right|_{0,\tau} = -\mathrm{Bi}_0\left(-\psi(0,\tau)\right), \quad \tau\geq 0\\
&\left.\frac{\partial\psi}{\partial\xi}\right|_{1,\tau} = -\mathrm{Bi}_l\left(\psi(1,\tau)\right), \quad \tau\geq 0.
\end{aligned} \tag{A.2}$$

The solution to the steady state subproblem (A.1)

is

$$\phi(\xi) = a\xi + b, \quad a = \mathrm{Bi}_0(b - \theta_0)$$
$$b = \frac{\theta_0}{1 + 1/\mathrm{Bi}_0 + 1/\mathrm{Bi}_l},$$

where the expressions for a and b follow from the boundary conditions and the fact that $\mathrm{Bi}_0\theta_0 + \mathrm{Bi}_l\theta_l = 0$.

Applying separation of variables to the transient subproblem (A.2) gives a solution of the form

$$\psi(\xi, \tau) = e^{-\omega^2\tau}\left[A\cos(\omega\xi) + B\sin(\omega\xi)\right],$$

where ω, A and B can be resolved from the initial and boundary conditions. The boundary condition at $\xi = 0$ gives $B = A\mathrm{Bi}_0/\omega$, and the boundary condition at $\xi = 1$ gives the transcendental equation

$$\cot(\omega) = \frac{\omega - \mathrm{Bi}_0\mathrm{Bi}_l/\omega}{\mathrm{Bi}_0 + \mathrm{Bi}_l} \tag{A.3}$$

for the eigenvalue ω. Equation (A.3) has an infinite number of solutions ω_n, where

$$\omega_1 \in (0, \pi),\ \omega_2 \in (\pi, 2\pi),\ \ldots$$
$$\omega_{-1} \in (-\pi, 0),\ \omega_{-2} \in (-2\pi, -\pi),\ \ldots,$$

and $\omega_{-n} = -\omega_n$. To build $\psi(\xi, \tau)$ by superposition, therefore, it suffices to take only the positive eigenvalues. Thus, the solution to subproblem (A.2) can be written as

$$\psi(\xi, \tau) = \sum_{n=1}^{\infty} A_n e^{-\omega_n^2\tau} X_n(\xi),$$

where $X_n(\xi) = \cos(\omega_n\xi) + (\mathrm{Bi}_0/\omega_n)\sin(\omega_n\xi)$. The ω_n can be computed by a nonlinear root-finding algorithm such as Newton's method.

It can be shown that the $X_n(\xi)$ are orthogonal:

$$m \neq n \quad \Longrightarrow \quad \int_0^1 X_m(\xi)X_n(\xi)\mathrm{d}\xi = 0.$$

To find the constants A_n, we use this orthogonality property and the initial condition

$$\phi(\xi) + \psi(\xi, 0) = 1$$
$$\Longleftrightarrow \quad \sum_{m=1}^{\infty} A_m e^{-\omega_m^2\tau} X_m(\xi) = 1 - \phi(\xi).$$

Multiplying both sides of this equation by $X_n(\xi)$ and integrating over ξ from 0 to 1 gives

$$\int_0^1 \sum_{m=1}^{\infty} A_m e^{-\omega_m^2\tau} X_m(\xi)X_n(\xi)\mathrm{d}\xi$$
$$= \int_0^1 (1 - \phi(\xi))X_n(\xi)\mathrm{d}\xi.$$

By orthogonality, therefore,

$$A_n = \frac{\int_0^1 (1 - \phi(\xi))X_n(\xi)\mathrm{d}\xi}{\int_0^1 X_n(\xi)^2\mathrm{d}\xi}.$$

Both of the integrals on the right-hand side have closed-form solutions. Plugging them in and simplifying gives equation (12).

Appendix B. Notation

Notation is summarized in Table B.2.

Table B.2: summary of notation.

Quantity	Symbol	Units	Dimensionless analog
Biot numbers	Bi_0, Bi_l	-	
Space coordinate	x	m	ξ
Time coordinate	t	s	τ
Temperature distribution	$T(x,t)$	K	$\theta(\xi,\tau)$
Thermal diffusivity	α	m^2/s	
Thermal conductivity	k	$\mathrm{W/m{\cdot}K}$	
Thickness	l	m	1
Driving temperatures	T_0, T_l	K	θ_0, θ_l
Heat transfer coefficients	h_0, h_l	$\mathrm{W/m^2{\cdot}K}$	
Temperature-independent fluxes	$\tilde{q}_0$, $\tilde{q}_l$	$\mathrm{W/m^2}$	
Net surface fluxes	$q_0(t)$, $q_l(t)$	$\mathrm{W/m^2{\cdot}K}$	
Lumped capacitance temperature	$T^{\mathrm{LC}}(t)$	K	$\theta^{\mathrm{LC}}(\tau)$
Spatial maximum temperature	$T_{\max}(t)$	K	
Alhama and Campo error	$\gamma_{\mathrm{AC}}(t)$	-	
Alhama and Campo error set	Γ_{AC}	-	
Spatial average temperature	$\bar{T}(t)$	K	$\bar{\theta}(\tau)$
Reference temperature	T_{ref}	K	0
Initial temperature	T_i	K	1
Time constant	t_c	s	τ_c
Surface temperature errors	$\gamma_0(t)$, $\gamma_l(t)$	-	
Spatial average temperature error	$\bar{\gamma}(t)$	-	
Steady state dimensionless temperature	$\phi(\xi)$	-	
Transient dimensionless temperature	$\psi(\xi,\tau)$	-	
n^{th} eigenfunction, coefficient, eigenvalue	$X_n(\xi)$, A_n, ω_n	-	
Time parameter	β	-	
Error threshold	δ	-	
Surface temperature error sets	Γ_0^δ, Γ_l^δ	-	
Spatial average temperature error set	$\bar{\Gamma}^\delta$	-	
All error set	Γ^δ	-	
Curve fit parameters	$a_{i\delta}$, $b_{i\delta}$, $c_{i\delta}$	-	